Biophysical Journal, Volume *114*

Supplemental Information

Response of Single Cells to Shock Waves and Numerically Optimized Waveforms for Cancer Therapy

Dongli Li, Antonio Pellegrino, Andre Hallack, Nik Petrinic, Antoine Jérusalem, and Robin O. Cleveland

SI: Response of Single Cells to Shock Waves and Numerically Optimized Waveforms for Cancer Therapy

Dongli Li, Antonio Pellegrino, Andre Hallack, Nik Petrinic, Antoine Jérusalem and Robin O. Cleveland

University of Oxford, Department of Engineering Science, Parks Rd., Oxford, OX1 3PJ, UK

1 Experimental setup

The experimental setup is described in Fig. 1, in which individual cells were embedded in a tissue-mimicking sample and their response to shock waves was visualised through an ultra-high speed imaging system.

1.1 Cell and tissue phantom preparation

Three human kidney epithelial cell lines were used in the experiments in order to compare the mechanical properties between invasive cancer cells and their non-cancerous counterparts. Normal cells were represented by human renal epithelial (HRE) cells (CC-2556, Lonza) which are primary cells isolated from human renal cortex and glomerular. Cancer cells were from clear cell carcinoma, CAKI-2 (ATCC HTB-47). Immortalised cells, which were transformed by HPV-16 virus, were used as the third cell line: HK-2 (ATCC CRL-2190). The three cell lines were routinely maintained in their corresponding culture medium in a cell culture incubator: BulletKit human renal cell system (Lonza) was used for HRE cells, McCoy's 5a Medium Modified (ATCC) and DMEM (Life Technology) both supplemented with 10% FBS and 1% antibiotic/antimycotic solution were used for CAKI-2 and HK-2 cells.

The day before experiments, cells from each cell line were trypsinized and resuspended in culture medium to a density of $\sim 0.1 \times 10^6$ cells/mL before being injected into a tissue-mimicking phantom. Each tissue-mimicking phantom consisted of 672 mg purified agarose powder (UltraPure Agarose, Invitrogen), 100 mL phosphate buffered saline (Gibco, ThermoFisher Scientific) and 112 mL of culture medium with resuspended cells ($\sim$1.2 million cells). The mixture was stirred gently at 37 °C and poured into a plexiglass mould, see Fig. 2, to set over 24 hours. The resulting phantoms had an elastic modulus of $\sim$10 kPa, similar to what would be expected for soft tissue [1, 2]. The cell density was chosen so that individual cells could be observed when subject to shock waves.

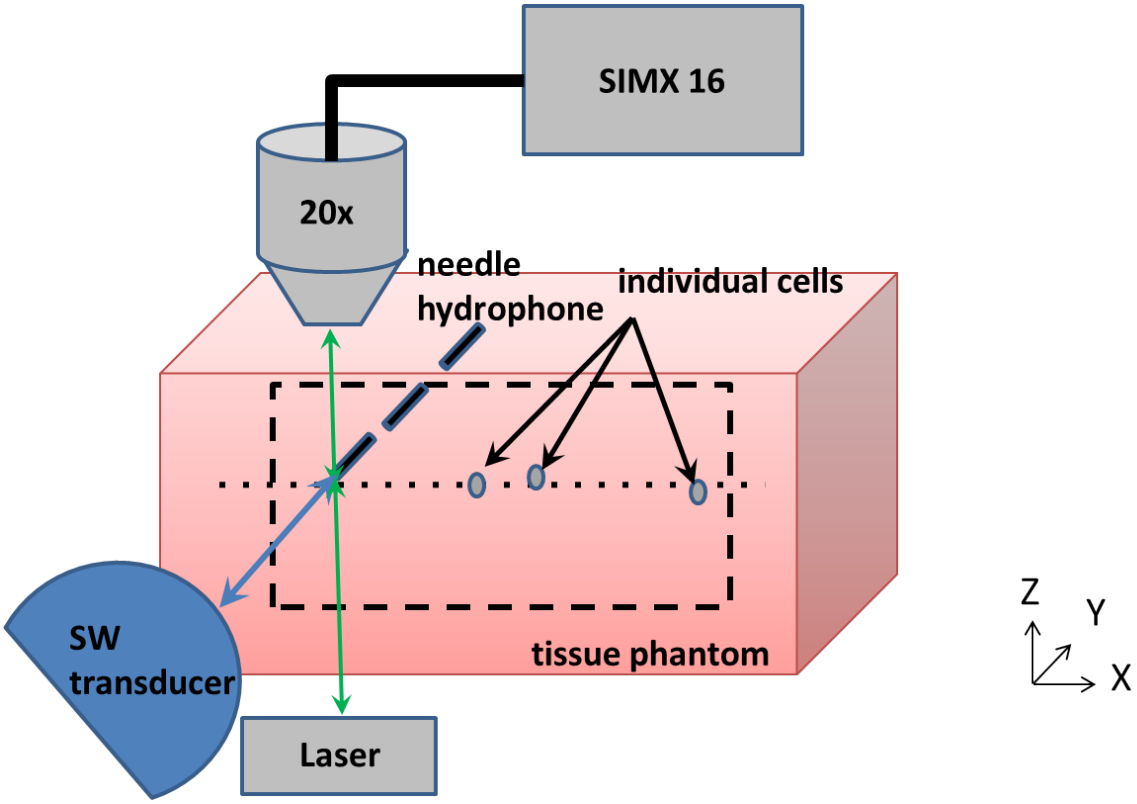

Fig. 1: Overview of the experimental setup containing a SIMX 16 ultra-high speed camera, a 20× microscopic objective, a laser source, a shock wave transducer, a needle hydrophone and a cell-agarose tissue phantom.

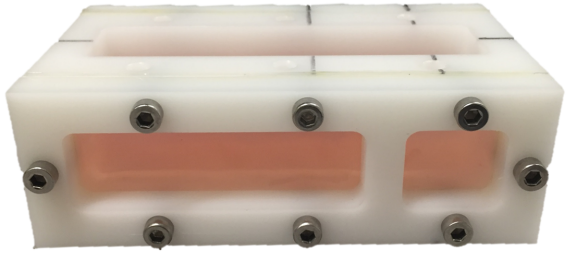

Fig. 2: Mould containing cell-agarose gel for carrying out shock wave exposure. The four transparent windows allow for imaging, lighting and applying shock waves simultaneously.

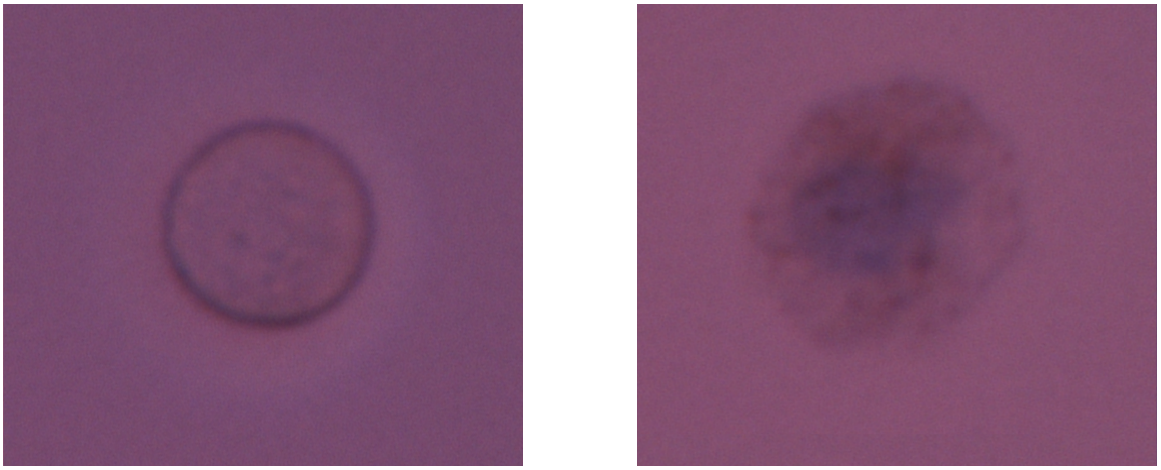

(a) (b)

Fig. 3: Examples of HK-2 cells (at 40× magnification) embedded in a 3D agarose tissue phantom: (a) a healthy cell with a well defined intact boundary; (b) a dead cell showing a diffuse boundary.

The viability of cells in the phantom was assessed by using a trypan blue solution (which selectively stains dead cells) 24 hours after they were embedded in the tissue phantom. Fig. 3(a) shows a healthy cell after 24 hours in agarose gel with a well defined boundary. In comparison Fig. 3(b) shows a cell that was non-viable, based on the blue stain, and also demonstrated a diffuse cell boundary. Fewer than 1% of cells were non-viable after 24 hours in agarose gel. The distinctive diffuse boundary was used to identify and exclude dead cells in the gel when high speed imaging was done.

1.2 Shock wave source

A clinical shock wave device (Minilith SL1-0G, Storz Medical AG) was used to generate shock waves. The Minilith employs an electromagnetic source and a parabolic reflector to effect focussing [3]. The focus occurs 50 mm from the face of the source and the focal zone is ellipsoidal in shape approximately 25 mm long in the axial direction by 2.4 mm in diameter.

Shock waves were measured inside the tissue phantoms using a fibre-optic probe hydrophone (FOPH) [4] based on a previously published design [5]. The FOPH measures light reflected from the tip of an optical fibre placed in the pressure field. As the pressure wave passes the fibre it causes a change in the refractive index of the

medium and hence changes the reflected light [5]. The FOPH employed here can measure acoustic pressures up to 100 MPa [4, 5].

The voltage output V from a photodetector is proportional to the light reflected at the fibre tip:

$$V(n) = gR(n) + S \tag{1}$$

where $R(n)$ is the reflectivity, g is the gain and S is the offset of the photodiode system (which were determined from measurements from known fluids). The reflectivity $R(n)$ is defined as:

$$R(n) = \left(\frac{n_f - n}{n_f + n}\right)^2 \tag{2}$$

where n_f is the index of refraction at the fibre (which is assumed to be constant in all conditions) and n is the index of refraction of the medium. The refractive index is related to the density through the Gladstone-Dale relation [6]:

$$\frac{n(t) - 1}{\rho(t)} = constant \tag{3}$$

With the known ambient conditions (n_0, ρ_0), the medium density can be inferred as:

$$\rho(t) = \rho_0 \frac{n(t) - 1}{n_0 - 1} \tag{4}$$

The density can be related to the pressure through the Tait equation of state,

$$p(\rho) = (Q + P_0)\left(\frac{\rho}{\rho_0}\right)^{\gamma} - Q \tag{5}$$

where $Q = 295.5$ MPa, $\gamma = 7.44$ for the conditions $T = 20$ °C, $P_0 = 100$ kPa and $\rho_0 = 1000$ kg/m^3 [5]. Therefore, using Equations (1)-(5), the pressure can be calculated from the voltage measured from the photodiode.

1.3 High speed camera and lighting source

An ultra-high speed camera (SIMX 16, Specialised Imaging) was used to image cells inside the gel. The camera has 16 CCD elements which can be triggered independently with a maximum frame rate of 200 million fps (i.e., 5 ns exposure time per frame). The camera was connected to a 20× microscopic objective (UMPLFLN20XW, Olympus) through a turning prism mirror (CM1-P01, Thorlabs) to magnify the region of interest and thus allow for close observation of a single cell (image resolution: 0.2 µm/pixel; field of view: 1.325 mm in diameter). All the connections between the microscopic objective and the camera were sealed to minimise interference from the ambient light.

The agar gel was backlit with a high speed visualisation laser (SI-LUX640, CAVITAR) which was fitted with a collimating lens. The visualisation laser was mounted onto a 3D microstage to align with the camera objective. The frame exposure time used in the experiment was 300 ns in order to observe the cell deformation as shorter times resulted in too little light to generate images of sufficient fidelity.

The camera and light source were triggered from the electromagnetic signal generated when the shock wave source was excited. For a target cells, high speed images were taken both in its reference state (i.e., before triggering shock waves) and during shock wave loading with the same imaging settings in order to measure the cell deformation in each image frame.

1.4 System alignment

The camera and shock wave source were aligned by placing a piezoelectric needle hydrophone (Müller Instruments) inside the gel coupled to the Minilith. The tissue sample was positioned such that a sharp image of the needle hydrophone was observed with the optimal light on the background. The Minilith was then manually adjusted until the pressure waveform matched a reference waveform for the focal spot. This aligned the optics and shock wave source. The gel was then translated laterally (without disturbing the position of the shock wave source or optics) until the needle was out of the region of interest and a cell could be observed. The optical system was finely adjusted (but still within the 2 mm focal spot of the shock source) to bring the cell sharply into focus.

2 Post-imaging analyses

Post-imaging analyses involved four image processing steps: image filtering, registration, automatic segmentation and feature extraction in order to determine cell boundaries. Area and perimeter measures were extracted from the cell boundary for quantitative analysis. The details of the steps are given below and the analysis was implemented in C++ and MATLAB.

2.1 Image denoising

Ultra-high speed images are generally noisy due to the low light levels, thus image filtering is desirable to allow for automatic cell contour segmentations. A non-local means (NL-means) filter [7] was applied to reduce noise while preserving the fine features of the original images. This algorithm takes advantage of the high degree of redundancy of images, i.e., images are constituted of patterns which are usually repetitive across itself [7]. Hence a noise reduced image can be reconstructed in which

the value of any pixel is estimated by all the pixels in its neighbourhood. This filtering technique is more advanced than other local smoothing methods or frequency domain filters as in the latter methods the relevant fine structures, details and texture of the original images are also smoothed out [7].

Given a noisy image v defined in a discrete gridded format I, the estimated value for pixel i is computed as a weighted average of all the pixels in the image [7]:

$$NL(v)(i) = \sum_{j \in I} w(i,j)v(j) \tag{6}$$

where the weights $w(i,j)$ depend on the similarity between the subsets around pixels i and j defined by the discrete grid:

$$w(i,j) = \frac{1}{Z(i)} e^{-\frac{\|v(N_i)-v(N_j)\|^2}{h^2}} \tag{7}$$

where the subset N_i is called the neighbourhood or similarity window of i (user-defined based on outcome quality and computational costs), $Z_i = \sum_j e^{-\frac{\|v(N_i)-v(N_j)\|^2}{h^2}}$ is the normalising factor and h is the parameter which controls the decay of the weight function.

The high speed images were firstly cropped to the region of the cell in order to improve the filter efficiency. The parameters used for the filter were optimised based on the balance between computational efficiency and filtering quality. The neighbourhood N was chosen to be 4×4 pixels, and the decay parameter $h = 100$. Fig. 4 shows an example of cell images before and after filtering. The NL-means algorithm filters out the background noise such as speckles and grids while retaining the relevant cell features.

2.2 Cell contour segmentation

The cell contour segmentation algorithm consists of an initial manual segmentation on the reference image (i.e., one of the 16 image frames taken before shock wave exposure), image registration process to propagate the initial segmentation contour to all the other high speed images, and the active contour segmentation algorithm to optimise the propagated segmentation results.

Image registration: Image registration was used to assist the process of segmentation of the cell contour on the high speed images. A high speed image sequence of a cell can be described as a set of images $I_n : \Omega \subset \mathbb{R}^2 \to \mathbb{R}$, $n \in \{1, ..., N\}$. For each of these images, there is a binary mask C_n which describes the cell contour.

Since this is a temporal sequence showing the motion of the same cell over time, it can be considered that each acquisition is equal to the first frame under a nonlinear

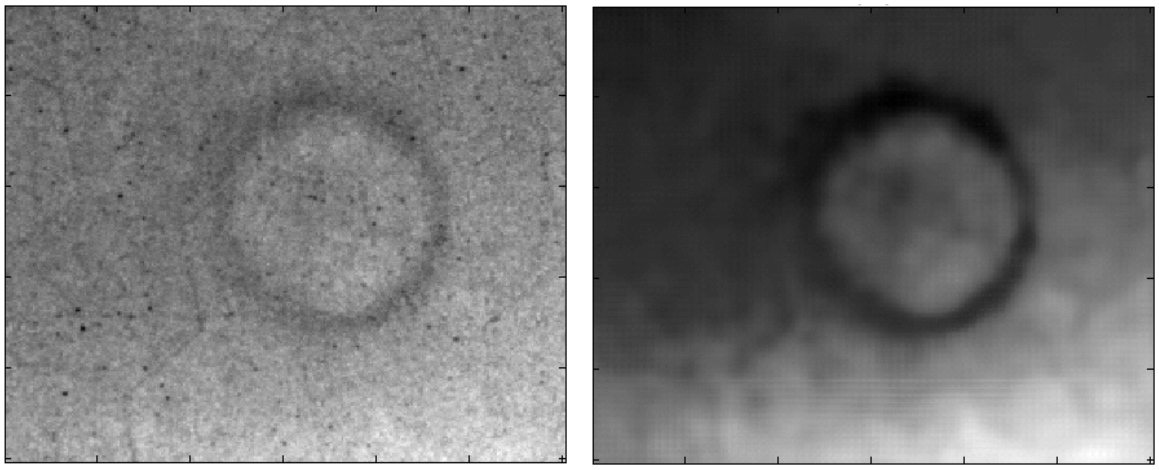

(a) (b)

Fig. 4: (a) Cropped raw image on the region of interest; (b) NL-means filtered image.

deformation field ϕ_n, an error term ϵ_n (related to noise and other artefacts), and a spatially varying multiplicative term K_n for illumination changes:

$$I_n = (I_1 K_n + \epsilon_n) \circ \phi_n \tag{8}$$

where $\circ$ is the operator that applies such deformation field. Consequently, given a contour for the first acquisition C_1, each subsequent contour is given by: $C_n = C_1 \circ \phi_n$. Image registration is used to estimate each of these deformation fields and hence propagate the initial contour to all frames. Its basic concept is to identify the optimal deformation field $\hat{\phi}_n$ based on an error metric E:

$$\hat{\phi}_n = \arg\min_{\phi_n} [E(I_1 \circ \phi_n, I_n)] \tag{9}$$

In this work, image registration was used to estimate the deformation fields and the estimation of the cell contours on image n was taken to be: $\hat{C}_n = C_1 \circ \hat{\phi}_n$.

The error measure E attempts to quantitatively evaluate the misalignment of both images, the most basic metric is the sum of square differences. However, the large changes of contrast in the images over the time sequence severely hinders its use as a measure of similarity for this problem. A similar challenge is found on liver ultrasound sequences, where occlusions lead to high contrast variability. For such case, the Scale Invariant Feature Transform (SIFT) has been used as similarity metric to great success [8]. It extracts features based on the gradient orientation profile of quadrants around each pixel of the images. These features are robust to illumination changes and are able to capture the main structural characteristics of the images.

The local mean square error of the feature vectors at each voxel can then be used as a robust measure of similarity.

The motion on the cells is expected to be smooth and without folding, hence, ϕ_n should be restricted to such deformation fields. Here we applied a logDemons framework which ensures that the obtained transformation fields are diffeomorphic, and thus satisfying the restrictions on the smooth deformation fields (no folding) [9]. It was combined with SIFT as a similarity metric in a multi-resolution application. It used three resolution levels, with 20 iterations at each level. The transformation field was smoothed at each iteration with $\sigma_{\text{diff}} = 2$ pixels. The SIFT Flow library was used for dense SIFT with its default parameters [10].

Active contour segmentation: Cell contours in each high speed image sequences were refined automatically using an active contour segmentation [11]. Any segmentation that was unsuccessful or visually unsatisfactory was then segmented manually with three repeats. An initial guess of the cell contour obtained from the initial manual segmentation and the image registration algorithm served as the input to the active contour segmentation algorithm. The active contour segmentation is an energy-minimising spline influenced by the image features and constrained by external forces which are user-defined in order to achieve the best contour segmentation results.

2.3 Feature extraction and analysis

The projected cell area, perimeter and centre of mass were determined from the cell contour segmentations, see Fig. 5. The cell area was estimated by counting the number of pixels within the cell contour and the cell perimeter was evaluated by summing up the distance between adjacent pixels on the contour.

Normalised area and perimeter changes at each imaging time point were defined by dividing the area or perimeter difference by their initial values at the reference state (i.e., before shock wave exposure), A_0 and P_0:

$$\begin{aligned} \frac{\Delta A}{A_0} &= \frac{A(t) - A_0}{A_0} \\ \frac{\Delta P}{P_0} &= \frac{P(t) - P_0}{P_0} \end{aligned} \tag{10}$$

where $A(t)$ and $P(t)$ are the measurements of area and perimeter respectively during shock wave exposure at time t. The shearing related perimeter change which excludes the effect of area change, $\Delta P_s(t) = P(t) - P_A(t)$, was analysed by comparing the deformed perimeter, $P(t)$, during shock waves to P_A, the expected perimeter change

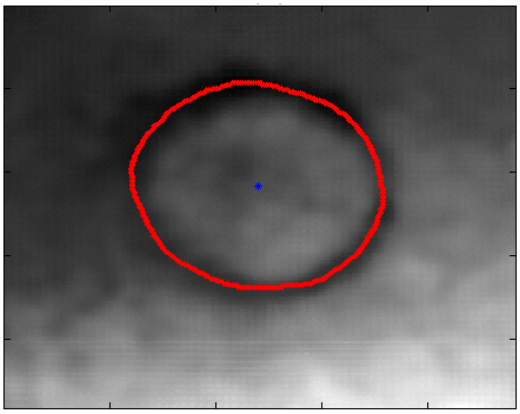

Fig. 5: An example of segmented cell showing the contour (red line) and centre of mass (blue dot).

due to the influence of area change for a circle:

$$P_A(t) = P_0\sqrt{\frac{A(t)}{A_0}} \tag{11}$$

Fig. 6 shows the relative shear perimeter change for the three cell types at all shock wave energy levels, revealing a value of less than 0.5%. This indicates that the perimeter change due to shearing was not detectable compared to the volumetric influence.

The image processing procedures described above are summarised in Fig. 7.

2.4 Segmentation variability

In order to quantify the variability in the segmentation process, a test was conducted on eight different cells per cell line subjected to shock waves with the three energy levels respectively. Each cell was manually segmented three times. The image processing algorithms were then performed on each manual cell segmentation in order to compare the measured area in each segmentation. The segmentation variability was defined as the variation of the measured area in the three segmentations. The test was repeated for each cell sample per cell line. Fig. 8 shows the segmentation variability of the three cell lines measured at shock wave energy level 8 where the greatest variance was found. In all cell samples the maximum area variability for the segmentation prior to the arrival of the shock waves was less than 0.2%. During shock loading, the majority of the cell samples exhibited less than 1% variability. In a few

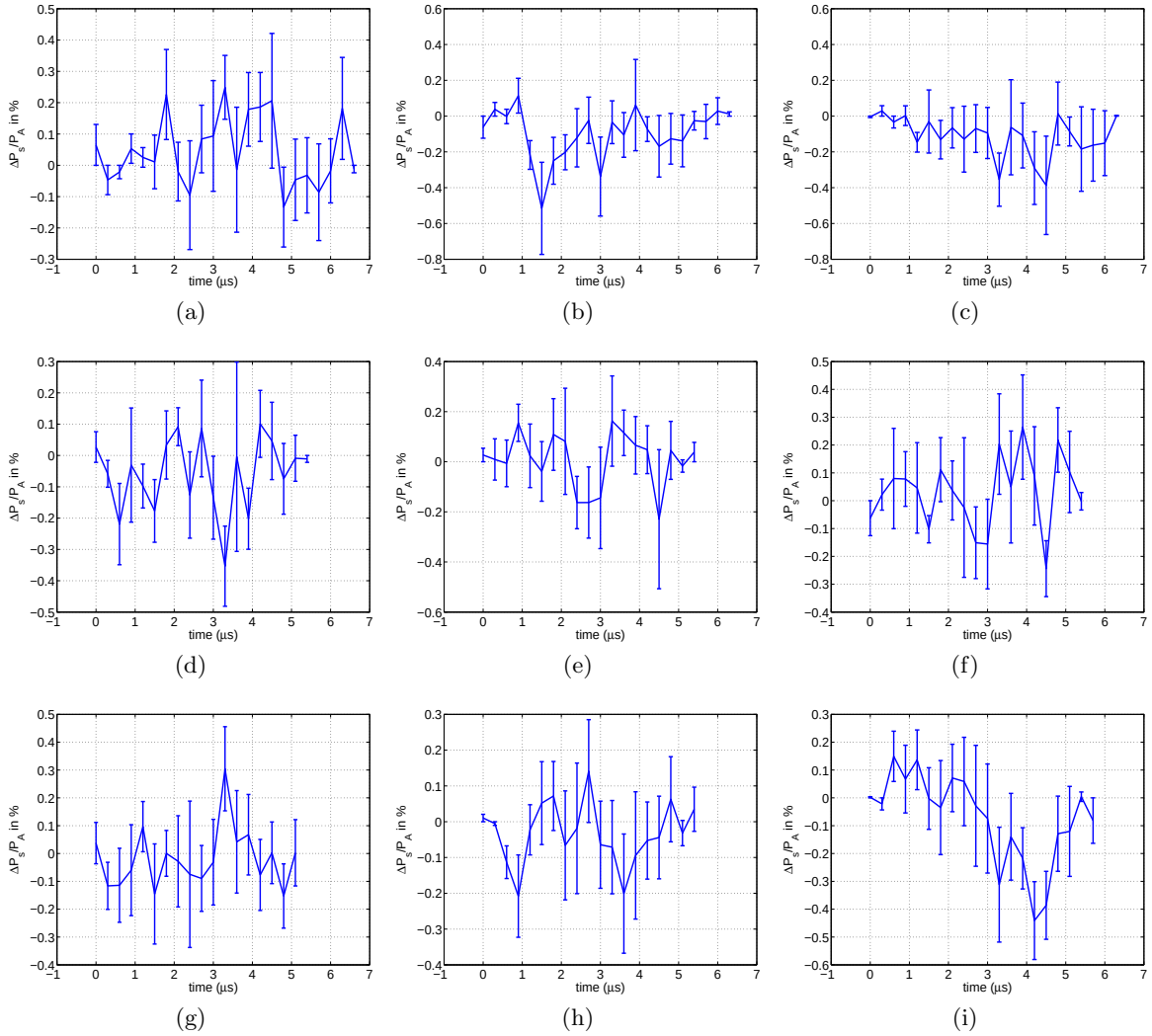

Fig. 6: The shear-related perimeter change for the three cell types: (a)-(c) HRE cells, (d)-(f) HK-2 cells, (g)-(i) CAKI-2 cells, at shock wave energy level 4 (a)(d)(g), 6 (b)(e)(h) and 8 (c)(f)(i).

cases a variability of 2-5% occurred during stretching, due to reduced image quality and thicker cell contours during the tensile phase of shock wave exposure.

2.5 Imaging variability

During the imaging process, the movement of the cells and the interaction between acoustics and optics may result in artefacts or interference in cell images leading to cell

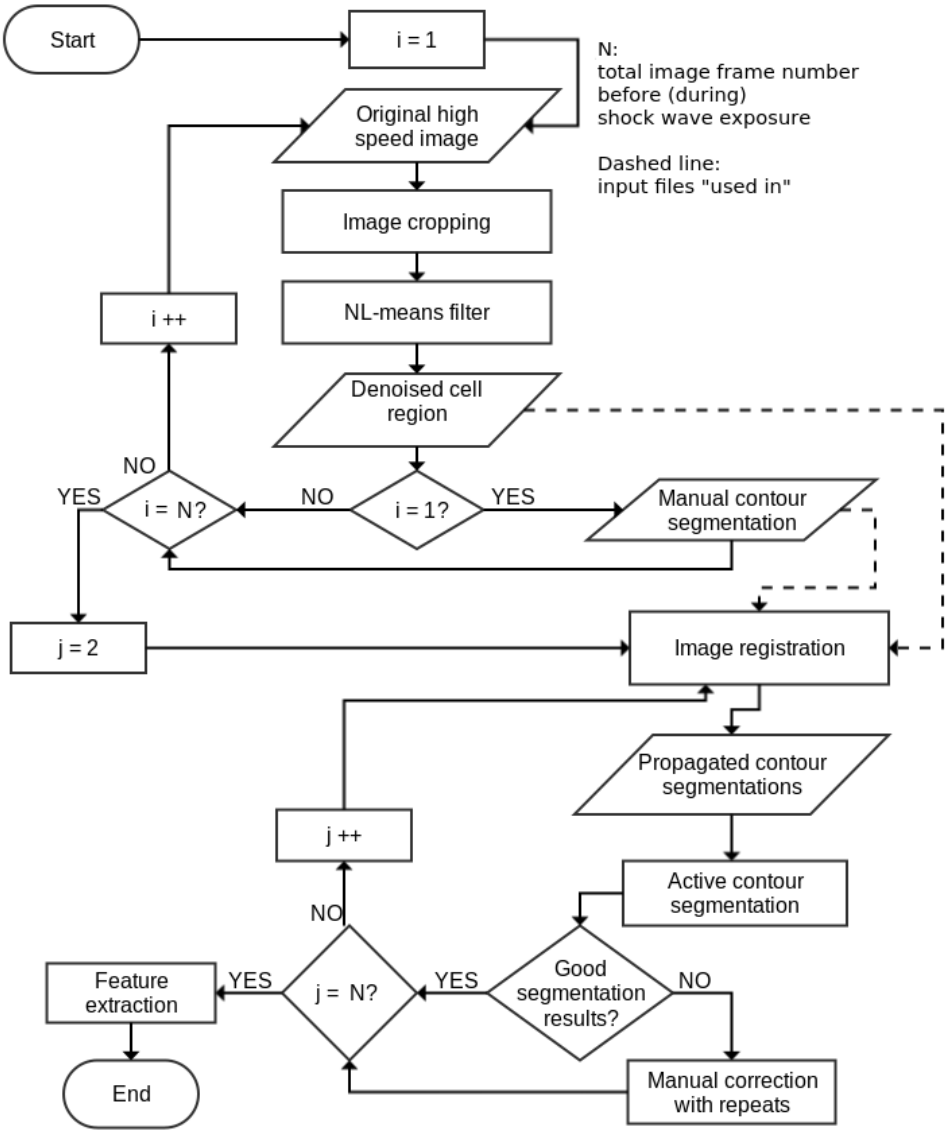

Fig. 7: Summary of the main procedures of cell image postprocessing.

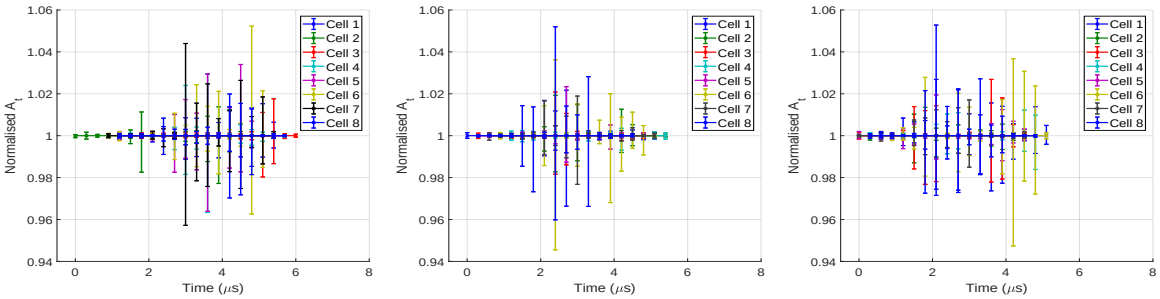

(a) (b) (c)

Fig. 8: The minimum and maximum segmented areas relative to the mean value of 8 cell samples taken at shock wave energy level 8 in (a) HRE cells; (b) HK-2 cells and (c) CAKI-2 cells.

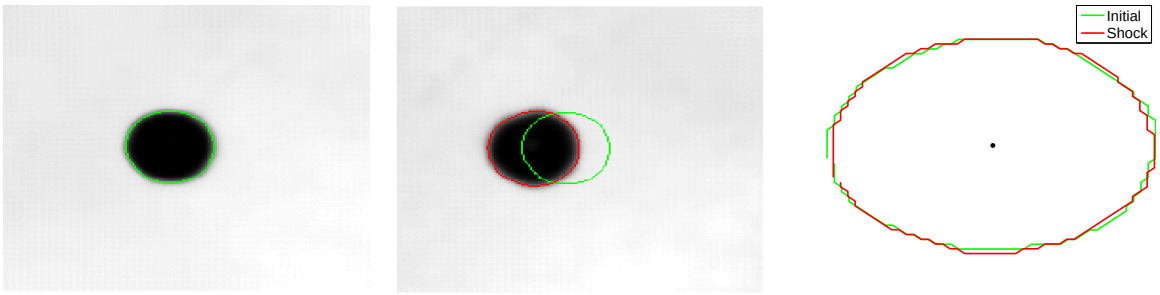

(a) (b) (c)

Fig. 9: An example of segmented microbeads at shock wave energy level 8. (a) before shock wave exposure; (b) during shock wave loading; (c) contour comparison.

contour change which is not due to the cell deformation in response to shock waves. Therefore, 10 µm polystyrene microspheres (Polybead, black, Polyscience Inc.) were used in the same experimental setting and post-imaging analysis was carried out in the same manner as for the cells. Due to the large bulk modulus of the microbeads (∼4 GPa [12]), shock waves should not lead to a detectable area change of the beads. Therefore, they can be used to assess the influence of acousto-optic effects, bead and gel movement, and image quality on the cell images.

Representative images and the segmentation of a microbead are presented in Fig. 9, it can be seen that the bead is translated but there is no significant change in its contour during shock wave exposure.

The area changes of the microbead contour measured at the three shock wave energy levels are presented in Fig. 10. The results showed that the area change of

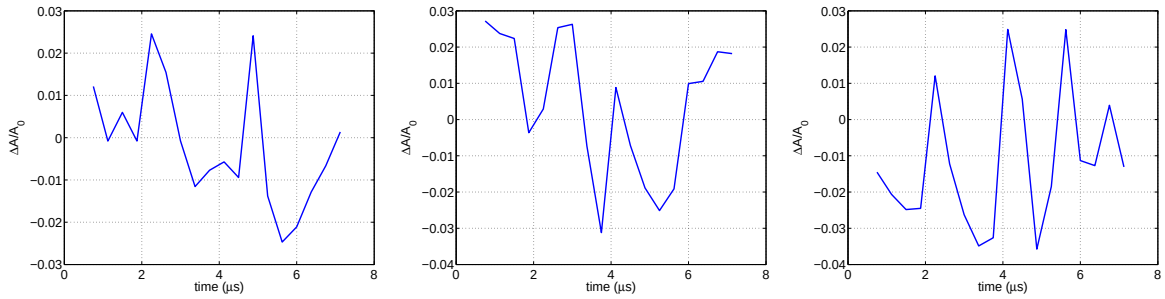

(a) (b) (c)

Fig. 10: Area change of the microbead contour at different shock wave energy levels (a) level 4; (b) level 6; and (c) level 8.

the 10 µm microbeads varied between -3% and 3% at the three shock wave energy levels. The mean error of area change found in the three shock wave energy levels (levels 4-8) were 0.1%, 0.4% and -1.1%, respectively. The area change of microbeads does not show a correlation with the shock wave profile whilst that of cells showed clear negative and positive phases of area change consistent with the compressive and tensile portions of the shock wave. This indicates that the imaging variability of microbeads may not be caused by shock wave interactions but the small movement of the objects inside the gel and segmentation variability.

3 Experimental results of cell deformation

Fig. 11 shows the maximum area increase changing with the shock wave energy levels: at energy level 4, the area increase in all three cell lines was found to be between 3.3% and 4.1%; at shock wave energy level 6, the area increase was between 6.3% and 8.5%; and at energy level 8, the maximum area increase was 17% in the HK-2 cells, 13% in HRE and 9% in CAKI-2. The difference was statistically significant for HK-2 and CAKI-2 cells with a p-value of less than 5% in the Mann-Whitney U test.

As a circle changes in radius from an initial radius r_0 to a different radius r_t, the area and perimeter are given by:

$$\begin{aligned} \frac{\Delta A}{A_0} &= \frac{2\pi\left(r_t^2 - r_0^2\right)}{2\pi r_0^2} \simeq \frac{4\pi r_0 \Delta r}{2\pi r_0^2} = \frac{2\Delta r}{r_0} \\ \frac{\Delta P}{P_0} &= \frac{2\pi\left(r_t - r_0\right)}{2\pi r_0} = \frac{\Delta r}{r_0} \end{aligned} \tag{12}$$

The ratio of the area change to perimeter change would therefore be a factor of two. Under the same area change, assuming the circle is gradually deforming to an ellipse,

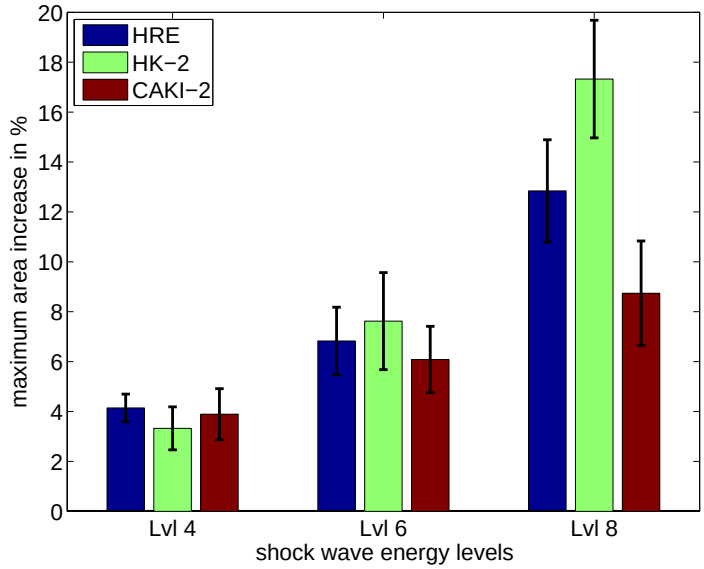

Fig. 11: The maximum area increase for the three cell types at three shock wave energy levels: (blue) HRE cells; (green) HK-2 cells and (red) CAKI-2 cells.

the area change over perimeter change is presented in Fig. 12, where b and a are the major and minor axes of an ellipse. For an ellipse with more than 10% axes length difference, the relative area change over relative perimeter change is less than 1.5.

Fig. 13 shows the ratio of the projected area change to perimeter change for all three cell types at the three different energy level settings. The ratio remained between 1.5 and 2 shows an axes difference less than 10% for an ellipse and suggests that the cells did not undergo substantial shear deformation during the shock wave exposure.

4 Cell viability test

A lactate dehydrogenase (LDH) assay was used to quantify cell viability inside the agarose gel. LDH is a cytosolic enzyme present in many different cell types. Cell membranes damaged by shock waves thus release LDH into the surrounding cell medium, which in turn can be quantified through enzymatic reaction and colorimetric detections. The level of LDH detected is directly proportional to cell damage, which indicates cell cytotoxicity [13]. In order to have sufficient cell density for the assay, the original sample mould (Fig. 1) was modified to concentrate cell populations to the shock wave focal zone in three cylindrical compartments (16 mm in diameter and 10 mm in height), see Fig. 14. Each compartment was filled with ∼500,000 cells homogenously embedded in the agarose gel with the same consistency as the rest of the tissue-mimicking phantom (0.6% agarose).

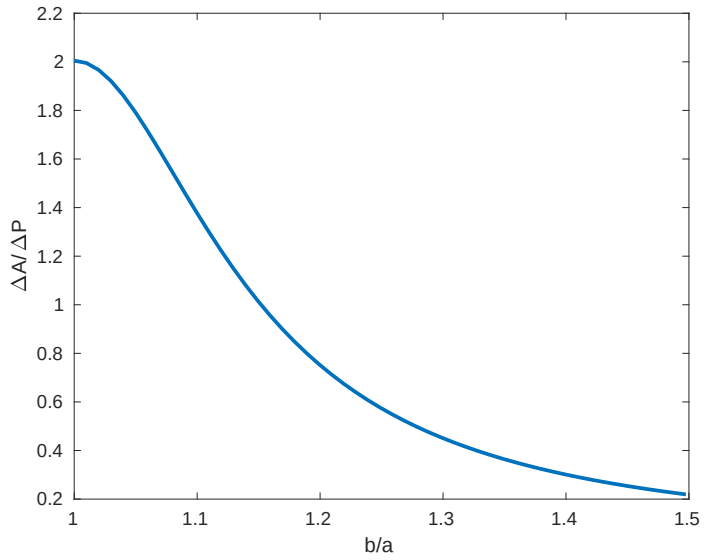

Fig. 12: The ratio of area change over perimeter change, where b/a is the ratio of the major over minor axis of an ellipse.

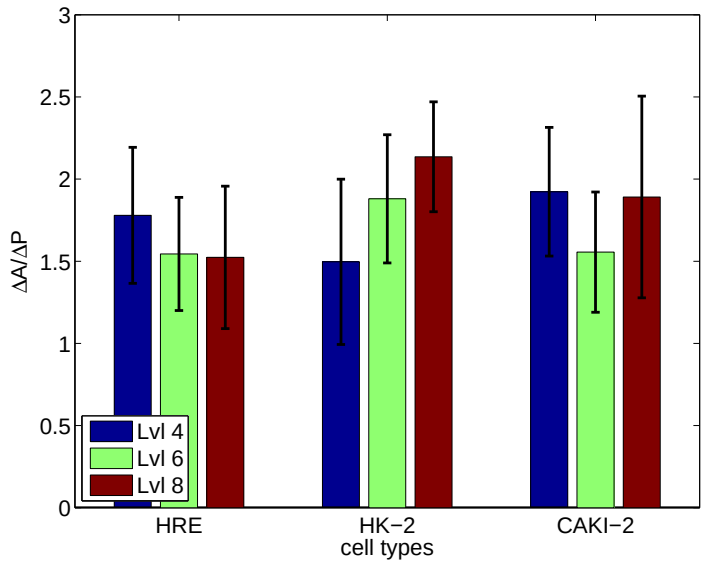

Fig. 13: The ratio between area change and perimeter change of single cell deformation in response to shock waves for the three cell lines: (blue) level 4; (green) level 6 and (red) level 8.

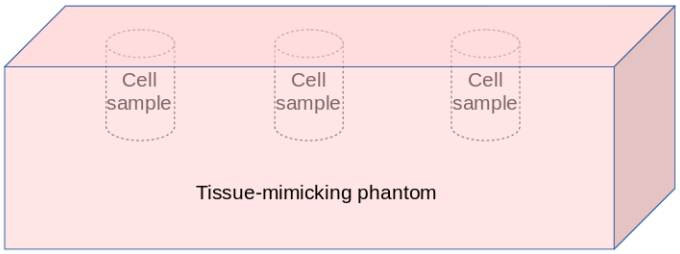

Fig. 14: Schematic of cell viability test samples.

The cell samples were treated with 500 shock waves at shock wave energy levels 4 and 8. At the same time, maximum LDH release control and sham control were included. A maximum LDH release control that represents the maximum cell cytotoxity was determined by lysing the cell sample before the gel set, while the sham control representing the maximum cell viability was determined by keeping the cell sample in the 37 °C incubator without shock wave treatments. The protocol is modified from reference [14].

After the shock wave treatments, the cell samples were carefully disected from the tissue phantom and placed in a 12-well plate filled with 2 mL cell medium. A complete medium control with only cell growth medium, no cells, was used to determine the background LDH activity due to the cell medium. The well plate was placed in the 37 °C incubator for 18 hours to allow the LDH to diffuse into the cell medium. Subsequently, 50 µL samples of the medium were collected from each well into a 96-well plate for LDH analysis using a LDH cytotoxicity assay kit (Pierce, ThermoFisher Scientific). The assay was performed by transferring 50 µL of reaction mixture to each sample well and mixing by gentle tapping. After incubating the plate at room temperature protected from light for 30 min, 50 µL stop solution was added to each sample well. The absorbance at 490 nm and 680 nm was measured using the FLUOstar Omega micro-plate reader to determine the LDH activity. The cell cytotoxicity was calculated as:

$$\%cytotoxicity = \frac{D_{sample} - D_{sham}}{D_{maxrelease} - D_{sham}} \times 100 \tag{13}$$

where D represents the absorbance measured at 490 nm subtracted from that at 680 nm.

5 Numerical modelling

5.1 Model geometry

Fig. 15 shows the 3D Finite Element model, which consists of a cell model of 20 µm in diameter embedded in a tissue model describing the surrounding extracellular matrix.

The shock wave profiles measured in the experiment were applied at the top surface

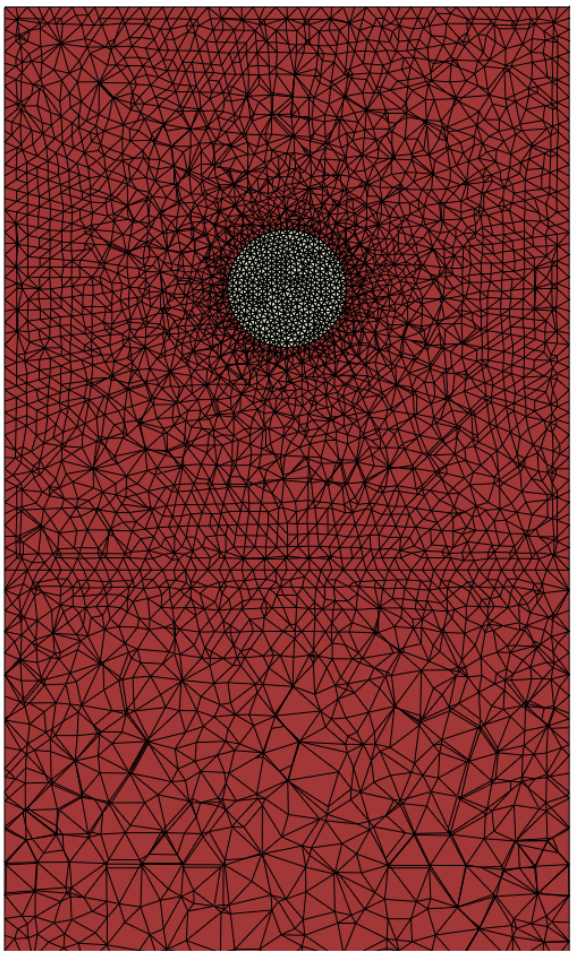

Fig. 15: Cross-sectional view from the mid-plane of the FE model (bottom truncated for presentation): a cell embedded in the surrounding tissue model.

of the model as an incident plane wave. The lateral boundaries were prohibited from moving laterally, and the bottom was fixed. The cell was positioned 50 µm from the top surface to minimise losses in the propagation of the incident wave, and the overall model length was taken to be 5 mm to ensure that wave reflections from the bottom boundary occurred only after the shock wave tail fully crossed the cell.

5.2 Constitutive framework

The conservation of linear momentum of a continuum system is described by:

$$\nabla \mathbf{P} + \rho_0 \mathbf{b} = \rho_0 \ddot{\mathbf{x}}, \qquad \forall \mathbf{X} \in B_0 \tag{14}$$

where $\mathbf{P}$ is the first Piola-Kirchhoff stress tensor which effectively relates force in the deformed configuration to area in the reference (undeformed) configuration B_0, ρ_0 is the density in B_0, $\mathbf{b}$ is the body force vector per unit mass, and $\mathbf{X}$ and $\mathbf{x}$ are the point coordinates vector in the reference and deformed configuration respectively.

The determination of the stress measure is also related to the deformation of the material of interest through its constitutive material law. The second Piola-Kirchhoff stress $\mathbf{S} = \mathbf{F}^{-1}\mathbf{P}$ and the Kirchhoff stress $\boldsymbol{\tau} = \mathbf{P}\mathbf{F}^T$ are also used in the description of the material laws. Here, $\mathbf{F} = \frac{\partial \mathbf{x}}{\partial \mathbf{X}}$ is the deformation gradient tensor and $J = det\,(\mathbf{F})$ is the Jacobian which represents the volumetric change with respect to the reference configuration. The cell deformation in the model was decomposed into a deviatoric response and a volumetric response, which are described below.

Nonlinear viscoelasticity: The deviatoric material response was described by a nonlinear viscoelasticity framework [15], where the deviatoric second Piola-Kirchhoff stress $\bar{\mathbf{S}}$ of the viscoelastic system (see Fig. 16) depends on the deviatoric initial elastic response $\bar{\mathbf{S}}^{\circ}$ and the evolution of the stress-like viscous internal variables $\mathbf{Q}_i$:

$$\bar{\mathbf{S}}(t) = \bar{\mathbf{S}}^{\circ}(t) - J^{-\frac{2}{3}}\mathrm{DEV}[\sum_{i=1}^{N} \mathbf{Q}_i(t)] \tag{15}$$

where N is the number of viscoelastic branches in Fig. 16; $N = 1$ for the first order generalised Maxwell viscoelastic model.

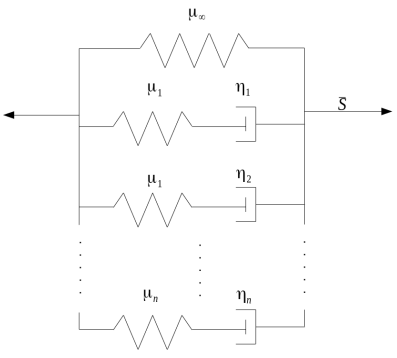

Fig. 16: Schematic of the viscoelasticity material framework in small deformation [15]

The deviatoric initial elastic stress is the derivative of the volume-preserving elastic stored energy function $\bar{W}^{\circ}$ with respect to the deviatoric right Cauchy-Green tensor $\bar{\mathbf{C}} = \bar{\mathbf{F}}^T\bar{\mathbf{F}}$ [15]:

$$\bar{\mathbf{S}}^{\circ}(t) = J^{-\frac{2}{3}}\mathrm{DEV}\{2\partial_{\bar{\mathbf{C}}}\bar{W}^{\circ}[\bar{\mathbf{C}}(t)]\} \tag{16}$$

where the operator "DEV" provides the correct notion of "deviatoric" stress tensor in terms of the right Cauchy-Green tensor $\mathbf{C}$, satisfying: $\mathbf{C}$**:**$\mathrm{DEV}[\bullet] = 0$.

The evolution of the internal variables is extended from the linear (small deformation) viscoelasticity case:

$$\begin{cases} \dot{\mathbf{Q}}_i(t) + \dfrac{1}{\tau_i}\mathbf{Q}_i(t) = \dfrac{\gamma_i}{\tau_i}\mathrm{DEV}\{2\partial_{\bar{\mathbf{C}}}\bar{W}^{\circ}[\bar{\mathbf{C}}(t)]\} \\ \lim\limits_{t\to\infty}\mathbf{Q}_i = \mathbf{0} \end{cases} \tag{17}$$

where $\tau_i = \eta_i/\mu_i$ is the relaxation time of each viscoelastic component and γ_i is the ratio of the shear modulus of each viscous component to the instantaneous shear modulus (i.e., $\gamma_i = \mu_i/\mu_0$).

After a few manipulations, the deviatoric Kirchhoff stress $\bar{\boldsymbol{\tau}}$ is given by:

$$\begin{aligned} \bar{\boldsymbol{\tau}}(t) =& \gamma_{\infty}\mathrm{dev}\{2\partial_{\bar{\mathbf{C}}}W^{\circ}[\bar{\mathbf{C}}(t)]\} \\ &+ \sum_{i=1}^{N}\gamma_i\mathrm{dev}\{\bar{\mathbf{F}}(t)\int_{-\infty}^{t}\exp[-(t-s)/\tau_i]\frac{d}{ds} \\ &\bar{\mathbf{F}}(s)^{-1}\mathrm{dev}\{2\partial_{\bar{\mathbf{C}}}\bar{W}^{\circ}[\bar{\mathbf{C}}(s)]\bar{\mathbf{F}}(s)^{-T}\}ds\bar{\mathbf{F}}(t)^T\} \end{aligned} \tag{18}$$

where "dev" is the deviator operator defined by: $\mathrm{dev}[\bullet] = (\bullet) - \frac{1}{3}[(\bullet):\mathbf{I}]\mathbf{I}$.

Equation of state: The volumetric Kirchhoff stress is given by $\boldsymbol{\tau}^{\circ}_{vol} = Jp\mathbf{I}$, where the pressure p captures the difference in bulk modulus under compression and tension. During compression the bulk modulus is taken to be K_C but during tension when the pressure exceeds the transition pressure threshold, $\tilde{p}$, the bulk modulus reduces to K_T (see Fig. 17):

$$\begin{aligned} p =& \mathrm{H}(\widetilde{p} - p)\left(K_T\frac{\rho-\rho_0}{\rho_0} + \Delta p\right) \\ &+ \mathrm{H}(p-\widetilde{p})\left(K_C\frac{\rho-\rho_0}{\rho_0}\right) - K_C\frac{\widetilde{\rho}-\rho_0}{\rho_0} \end{aligned} \tag{19}$$

where H is the Heaviside function, $\Delta p = (K_C - K_T)(\widetilde{\rho}-\rho_0)/\rho_0$, $\widetilde{p}$ and $\widetilde{\rho}$ are the transition pressure and density, respectively. The compressive bulk modulus K_C was determined to be 2 GPa due to small cell deformation under compression and high

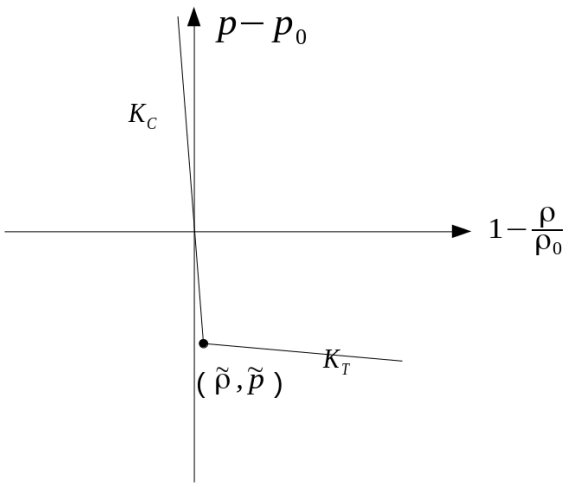

Fig. 17: Schematic of the bilinear EoS accounting for different bulk moduli for the compressive (K_C) and tensile phases (K_T) of shock waves. $\tilde{\rho}$ and $\tilde{p}$ are the density and pressure at the transition, and p_0 and ρ_0 refer to their reference states.

water content of the cell, whilst the other parameters (K_T and $\tilde{p}$) were calibrated against experimental observations.

Artificial viscosity: In a discretised scheme, such as in the finite element method, artificial viscosity is necessary to spread the shock front over several elements so that the simulation of shock fronts (with length scale a prori less than the mesh size) can be captured without introducing spurious oscillations. The spurious oscillations can be eliminated by subtracting a certain amount of pressure p_{av} from the original pressure loadings [16], where p_{av} is expressed as:

$$p_{av} = \rho l_e \dot{\epsilon_v} (b_1 c_d + l_e {b_2}^2 \dot{\epsilon_v}) \tag{20}$$

where b_1 and b_2 are the linear and quadratic damping coefficients, respectively, l_e is the characteristic element size, $\dot{\epsilon_v}$ is the volumetric strain rate and c_d is the longitudinal wave (p-wave) speed.

5.3 Numerical model calibration and validation

The material properties (K_T and $\tilde{p}$) in the constitutive framework of each cell model were calibrated against the experimental data by finding the least mean square error between the simulation and experimental results in terms of the area change for all the three shock wave loading conditions. This process was cross-validated by determining the optimal values for only two of the energy level settings at a time and testing for the

"left out" (untrained) energy setting by analysing the difference between its simulation and experimental results using the previously calibrated values. Table 1 lists the cross-validation results for each cell line, including different training combinations, resultant calibration values and error between simulation and experimental results in the untrained data set. The calibration process of the numerical model presents an error around 12% for all cell types, which is acceptable considering the small compressive deformation and the experimental variation, see Fig. 3 in the main article. It can also be seen that the transition pressure values obtained for healthy (HRE and HK) cells are consistently larger in magnitude compared to that of cancer (CAKI) cells. This indicates a physical difference in transition pressure between two groups which is highlighted by performing a Welch's t-test with a p value less than 0.1.

Table 1: Cross-validation of the numerical model for the three cell lines.

Cell type	Trained settings	Optimal properties		Untrained setting	error	mean error
		K_T	$\tilde{p}$			
HRE	Lvl 4 & Lvl 6	20MPa	-4.6MPa	Lvl 8	6.8%	
	Lvl 4 & Lvl 8	25MPa	-4.4MPa	Lvl 6	17.9%	
	Lvl 6 & Lvl 8	20MPa	-5.2MPa	Lvl 4	12.4%	12.4%
HK	Lvl 4 & Lvl 6	20MPa	-4.6MPa	Lvl 8	7.7%	
	Lvl 4 & Lvl 8	20MPa	-4.6MPa	Lvl 6	9.5%	
	Lvl 6 & Lvl 8	19MPa	-4.4MPa	Lvl 4	19.8%	12.3%
CAKI	Lvl 4 & Lvl 6	22MPa	-4.4MPa	Lvl 8	13.7%	
	Lvl 4 & Lvl 8	35MPa	-4MPa	Lvl 6	8.1%	
	Lvl 6 & Lvl 8	35MPa	-3.8MPa	Lvl 4	14.1%	12.0%

5.4 Quantification of stress and strain evolution of cells

Fig. 18 shows the comparison of the simulated pressure waveforms obtained at the centre of each cell model at the three shock wave energy levels. The maximum pressure differences among the three cell lines were 7%, 3% and 5% corresponding to shock wave energy level 4, 6 and 8, respectively. This shows that the shock wave propagation is not strongly influenced by the difference in mechanical properties between the cell types. The maximum von Mises stress, which quantifies the amount of shearing in the model, was found to be of the order of 100 Pa measured at the cell equator using the deviatoric mechanical properties from the literature.

The membrane strain in each cell line at different shock wave energy levels is depicted in Fig. 19. The membrane strain is defined by the ratio of the difference in

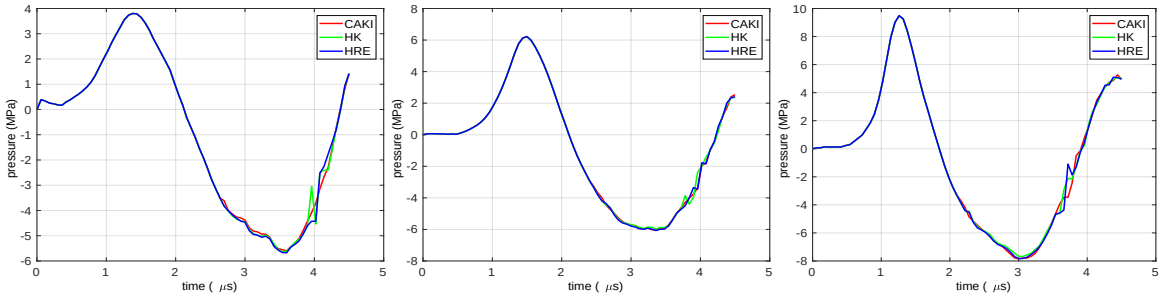

(a) (b) (c)

Fig. 18: Comparison of the simulated pressure measured in the centre of the cell models: (a) level 4; (b) level 6; (c) level 8; CAKI-2 cells (red); HK-2 (green) and HRE (blue).

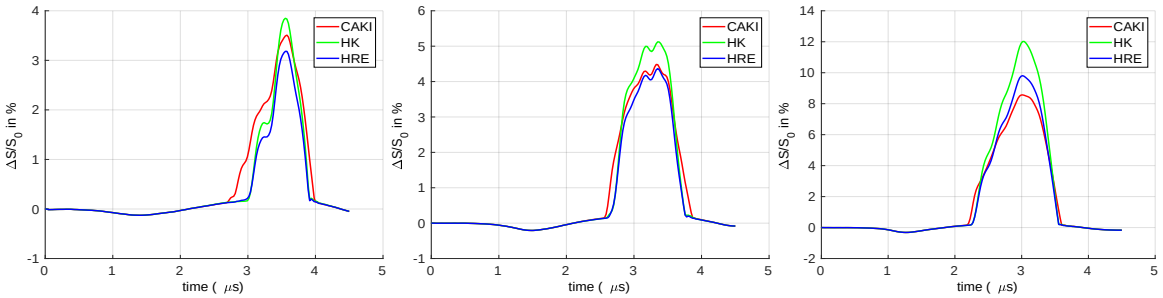

(a) (b) (c)

Fig. 19: The overall simulated cell membrane strain: (a) level 4; (b) level 6; (c) level 8; CAKI-2 cells (red); HK-2 (green) and HRE (blue).

the cell membrane surface area to the initial value at the reference state, S_0:

$$\frac{\Delta S}{S_0} = \frac{S(t) - S_0}{S_0} \tag{21}$$

where $S(t)$ is the surface area of the cell membrane during shock wave exposure at time t. The results show greater variation than the pressure waveforms. The maximum membrane area expansion under tension reached up to 10% in HRE, 12% in HK-2 and 8.5% in CAKI-2 cells at shock wave energy level 8.

References

1. G. E. Leclerc, L. Debernard, F. Foucart, L. Robert, K. M. Pelletier, F. Charleux, R. Ehman, and H. B. Tho, "Characterization of a hyper-viscoelastic phantom mimicking biological soft tissue using an

abdominal pneumatic driver with magnetic resonance elastography (mre)," *Journal of Biomechanics*, vol. 45, no. 6, pp. 952–957, 2012.
2. S. F. Bensamoun, L. Robert, G. E. Leclerc, L. Debernard, and F. Charleux, "Stiffness imaging of the kidney and adjacent abdominal tissues measured simultaneously using magnetic resonance elastography," *Clinical Imaging*, vol. 35, no. 4, pp. 284–7, 2011.
3. O. Wess, *Extracorporeal Shock Wave Therapy (ESWT) in Orthopaedics and Traumatology. User Manual.*
4. M. R. Betney, R. A. Roy, and Y. Ventikos, "Computational and experimental study of intense shock-cavity interactions," Ph.D. dissertation, University of Oxford, 2015.
5. J. Parsons, C. Cain, and J. B. Fowlkes, "Cost-effective assembly of a basic fiber-optic hydrophone for measurement of high-amplitude therapeutic ultrasound fields," *The Journal of the Acoustical Society of America*, vol. 119, no. 3, pp. 1432–40, 2006.
6. J. H. Gladstone and T. P. Dale, "Researches on the refraction, dispersion, and sensitiveness of liquids," *Philosophical Transactions of the Royal Society of London*, vol. 153, no. 1863, pp. 317–343, 1863.
7. A. Buades, B. Coll, and J. M. Morel, "A review of image denoising algorithms, with a new one," *Society of Industrial and Applied Mathematics*, vol. 4, no. 2, pp. 490–530, 2005.
8. A. Hallack, B. W. Papiez, A. Cifor, M. J. Gooding, and J. A. Schnabel, "Robust liver ultrasound tracking using dense distinctive image features," in *Challenge on Liver Ultrasound Tracking CLUST 2015*, 2015.
9. T. Vercauteren, X. Pennec, A. Perchant, and N. Ayache, "Symmetric log-domain diffeomorphic registration: a demons-based approach," *MICCAI*, 2008.
10. C. Liu, J. Yuen, and A. Torralba, "SIFT flow: Dense correspondence across scenes and its applications," *IEEE Transactions on Pattern Analysis and Machine Intelligence*, vol. 33, no. 5, 2011.
11. M. Kass, A. Witkin, and D. Terzopoulos, "Snakes - active contour models," *International Journal Of Computer Vision*, pp. 321–331, 1987.
12. P. Mott, J. Dorgan, and C. Roland, "The bulk modulus and poisson's ratio of incompressible materials," *Journal of Sound and Vibration*, vol. 312, no. 4-5, pp. 572–575, 2008.
13. Thermo Scientific, *Pierce LDH Cytotoxicity Assay Kit, User Manual.*
14. S. Nwokeoha, "Lithotripter shock wave induced rna-based gene therapy," Ph.D. dissertation, University of Oxford, 2018.
15. J. Simo and T. Hughes, *Computational inelasticity.* Springer, 2008.
16. *Abaqus user manual 6.12*, 2012.